

The Discontinuous Galerkin Time-Domain method for Maxwell's equations with anisotropic materials

Michael König^{*}, Kurt Busch, Jens Niegemann

Institut für Theoretische Festkörperphysik and DFG-Center for Functional Nanostructures (CFN), Karlsruhe Institute of Technology (KIT), Wolfgang-Gaede Str. 1, 76128 Karlsruhe, Germany

Received 25 January 2010; received in revised form 1 April 2010; accepted 1 April 2010
Available online 13 April 2010

Abstract

The Discontinuous Galerkin method is an accurate and efficient way to numerically solve the time-dependent Maxwell equations. In this paper, we extend the basic, two-dimensional formulation for isotropic materials to allow anisotropic permittivity tensors. Using a reference system with an analytical solution, we demonstrate that our extensions do not alter the superior convergence characteristics of the fundamental algorithm. We further apply our method to cylindrical invisibility cloaks to investigate the performance which can be achieved in experiments.

© 2010 Elsevier B.V. All rights reserved.

Keywords: Discontinuous Galerkin method; Anisotropic materials; Time-domain; Maxwell's equations

1. Introduction

Scientists and engineers in the photonics community use numerical simulations on a daily basis to design new devices, optimize existing ones, and explain findings in their experiments. The demands simulation tools have to face are simply stated, but difficult to fulfil. The results should be accurate with only moderate requirements concerning computational resources. Besides tools specialised for certain problem classes, a number of general purpose solvers have gained popularity, as they can treat a variety of different systems within the same framework. Among these, we find the widely used Finite-Difference Time-Domain (FDTD) algorithm and Finite Element Methods (FEM).

FDTD is a very fast and simple solver for the time-domain formulation of Maxwell's equations [1].

However, the simplicity comes at the price of only second-order accuracy. In addition, one is restricted to an inflexible orthogonal spatial discretisation, the so-called Yee-grid. On the other hand, FEM allows a flexible discretisation of the physical system in order to resolve small geometrical features or curved shapes [2]. Furthermore, the spatial order of accuracy can be improved by using higher order basis functions. Then again, conventional FEM strongly relies on the solution of a sparse system of linear equations. Thus, it suffers from a large computational overhead as compared to FDTD, rendering FEM cumbersome for time-domain computations.

In 2002, Hesthaven and Warburton adapted the Discontinuous Galerkin Time-Domain (DGTD) method to electrodynamics [3,4]. In principle, DGTD is a variant of conventional FEM. The main difference is that the basis functions are only defined on a single element without any overlap with the neighbouring elements. This effectively decouples the elements. After having performed all expensive operations on each

^{*} Corresponding author.

E-mail address: mkoenig@tfp.uni-karlsruhe.de (M. König).

element separately, the coupling between the elements is reintroduced via the so-called numerical flux. With this trick, the mathematical complexity is significantly reduced, thus allowing DGTD to effectively treat time-dependent problems.

Until now, however, most formulations of the DGTD method were restricted to isotropic – and in some cases dispersive – materials [3,5–8]. This excludes a wide class of interesting materials and related physics. For example, anisotropic materials provide a way to achieve so-called invisibility cloaking using carpets, cylindrical structures or more general geometries [9–11]. The treatment of anisotropic materials within a DGTD approach was discussed in Ref. [12], where the authors employed a so-called central flux to interconnect neighbouring elements. However, a central flux may reduce the accuracy because spurious modes are not sufficiently damped. Furthermore, it may introduce instabilities when used in combination with perfectly matched layers [13]. In this paper, we extend the DGTD method to anisotropic materials and derive an upwind flux for two-dimensional systems. We validate the resulting algorithm using an analytical reference solution. Finally, we present simulations of cylindrical cloaking structures.

2. The Discontinuous Galerkin method

To simplify the problem, we restrict ourselves to the important case of two-dimensional systems in TE-polarisation, i.e., the only non-vanishing components of the electromagnetic fields are E_x , E_y , and H_z . Furthermore, we assume an anisotropic permittivity tensor:

$$\underline{\epsilon} = \begin{pmatrix} \epsilon_{xx} & \epsilon_{xy} \\ \epsilon_{yx} & \epsilon_{yy} \end{pmatrix}$$

and an isotropic permeability μ . The derivation is roughly divided into two parts. First, a semi-discrete form, i.e., a form where the spatial derivatives are discretised, of Maxwell's curl equations is derived. Secondly, we solve the Riemann problem for anisotropic materials to get the correct expression for the numerical flux. As the first part of the derivation is very similar to – and shares notation with – the one presented in Ref. [7], we briefly repeat the key ideas and state the final result.

We start by tessellating the two-dimensional computational domain into elements, e.g., triangles. Then, we multiply Maxwell's curl equations in conservation form by Lagrange polynomials $L_i(\vec{x})$ and integrate over an

individual element Ω^k . Integration by parts of the resulting integral yields a surface integral over the flux \vec{F} through the element boundary. Replacing this flux by the numerical flux \vec{F}^* and reversing the integration by parts yields

$$\begin{aligned} & \int_{\Omega^k} (\mathcal{Q} \partial_t \mathbf{q} + \nabla \cdot \vec{F}(\mathbf{q})) L_i(\vec{r}) d\vec{r} \\ &= \int_{\partial\Omega^k} \hat{n} \cdot (\vec{F}(\mathbf{q}) - \vec{F}^*(\mathbf{q})) L_i(\vec{r}) d\vec{r} \end{aligned}$$

as an intermediate result. Here, \hat{n} is the outwardly directed normal vector of the element and we have defined:

$$\mathcal{Q}(\vec{r}) = \begin{pmatrix} \epsilon & 0 \\ 0 & \mu \end{pmatrix}, \quad \mathbf{q}(\vec{r}, t) = \begin{pmatrix} E_x \\ E_y \\ H_z \end{pmatrix}, \quad \text{and}$$

$$\hat{n} \cdot \vec{F}(\vec{r}, t) \equiv \begin{pmatrix} -n_y H_z \\ n_x H_z \\ n_x E_y - n_y E_x \end{pmatrix}.$$

If we expand the electromagnetic fields in terms of time-dependent expansion coefficients and space-dependent Lagrange polynomials $L_j(\vec{x})$, the time and space variables separate. After introducing differentiation matrices \mathcal{D}_x^k and \mathcal{D}_y^k , the mass matrix \mathcal{M}^k , and the face matrix \mathcal{F}^k on the element Ω^k , we obtain:

$$\begin{aligned} \partial_t E_x^k &= \eta_{xx} \mathcal{D}_y^k H_z^k - \eta_{xy} \mathcal{D}_x^k H_z^k + (\mathcal{M}^k)^{-1} \mathcal{F}^k \\ &\quad \times (\eta_{xx} [\hat{n} \cdot (\vec{F} - \vec{F}^*)]_x + \eta_{xy} [\hat{n} \cdot (\vec{F} - \vec{F}^*)]_y) \\ \partial_t E_y^k &= \eta_{yx} \mathcal{D}_y^k H_z^k - \eta_{yy} \mathcal{D}_x^k H_z^k + (\mathcal{M}^k)^{-1} \mathcal{F}^k \\ &\quad \times (\eta_{yx} [\hat{n} \cdot (\vec{F} - \vec{F}^*)]_x + \eta_{yy} [\hat{n} \cdot (\vec{F} - \vec{F}^*)]_y). \end{aligned}$$

The definitions of the matrices are given in Ref. [7] and shall not be repeated here. The variables E_x^k , E_y^k , and H_z^k represent the expansion coefficients of the respective electromagnetic field components. Furthermore, we have defined:

$$\underline{\eta} = \begin{pmatrix} \eta_{xx} & \eta_{xy} \\ \eta_{yx} & \eta_{yy} \end{pmatrix} \equiv \underline{\epsilon}^{-1}$$

as the inverse permittivity. As the permeability μ is still assumed to be a scalar quantity, the semi-explicit form for $\partial_t H_z^k$ is identical to the isotropic case (see Ref. [7]).

3. An upwind flux for anisotropic materials

To complete our extension to anisotropic materials, we have to obtain an upwind expression for $\hat{n} \cdot (\vec{F} - \vec{F}^*)$. To this end, we have to solve the Riemann

problem [4,14]:

$$\begin{aligned} c^- \mathcal{Q}^-(\mathbf{q}^- - \mathbf{q}^*) + \hat{n} \cdot (\vec{F}^- - \vec{F}^*) &= 0 \\ \hat{n} \cdot (\vec{F}^* - \vec{F}^{**}) &= 0 \\ -c^+ \mathcal{Q}^+(\mathbf{q}^+ - \mathbf{q}^{**}) + \hat{n} \cdot (\vec{F}^+ - \vec{F}^{**}) &= 0, \end{aligned}$$

where

$$c^\pm = \sqrt{\frac{\hat{n}^T \underline{\epsilon}^\pm \hat{n}}{\mu^\pm \cdot \det(\underline{\epsilon}^\pm)}} \quad (1)$$

denotes the speed with which a wave travels along the direction of the unit normal. The superscript “-” (“+”) denotes quantities within the local (neighbouring) element. We note that $\vec{F}^- \equiv \vec{F}$. After some tedious algebraic manipulations we find:

$$H_z^- - H_z^* = \frac{1}{d} \cdot \begin{pmatrix} c^- \cdot \det(\underline{\epsilon}^-) \cdot \hat{n}^T \underline{\epsilon}^+ \hat{n} \cdot \Delta H_z \\ -c^- c^+ (\underline{\epsilon}^-) \cdot \det(\underline{\epsilon}^+) (\hat{n} \times \Delta \vec{E})_z \end{pmatrix}$$

and

$$\begin{aligned} &(\hat{n} \cdot [\vec{F}^- - \vec{F}^*])_z \\ &= \frac{c^- \mu^- (\hat{n} \times \Delta \vec{E})_z - c^- c^+ \mu^- \mu^+ \Delta H_z}{c^- \mu^- + c^+ \mu^+}, \end{aligned}$$

where

$$\begin{aligned} \Delta H_z &= H_z^- - H_z^+, \\ \Delta \vec{E} &= (E_x^- - E_x^+) \cdot \hat{e}_x + (E_y^- - E_y^+) \cdot \hat{e}_y, \end{aligned}$$

and

$$d = c^- \cdot \det(\underline{\epsilon}^-) \cdot (\hat{n}^T \underline{\epsilon}^+ \hat{n}) + c^+ \cdot \det(\underline{\epsilon}^+) \cdot (\hat{n}^T \underline{\epsilon}^- \hat{n}).$$

This intermediate result can be simplified by eliminating $\det(\underline{\epsilon}^\pm)$ and $\hat{n}^T \underline{\epsilon}^\pm \hat{n}$ using the square of (1). Finally, the numerical flux reads:

$$\begin{aligned} &\hat{n} \cdot (\vec{F}^- - \vec{F}^*) \\ &= \begin{pmatrix} \frac{-n_y}{Z^+ + Z^-} (Z^+ \Delta H_z - [n_x \Delta E_y - n_y \Delta E_x]) \\ \frac{n_x}{Z^+ + Z^-} (Z^+ \Delta H_z - [n_x \Delta E_y - n_y \Delta E_x]) \\ \frac{1}{Y^+ + Y^-} (Y^+ [n_x \Delta E_y - n_y \Delta E_x] - \Delta H_z) \end{pmatrix}, \quad (2) \end{aligned}$$

where we have defined $Z^\pm = \mu^\pm c^\pm$ and $Y^\pm = (Z^\pm)^{-1}$. Comparing Eq. (2) with the result for the numerical flux in isotropic media (see Ref. [7]), we note that the permittivity tensor modifies the flux only via c^\pm . Thus, concerning the numerical flux, we can define an effective

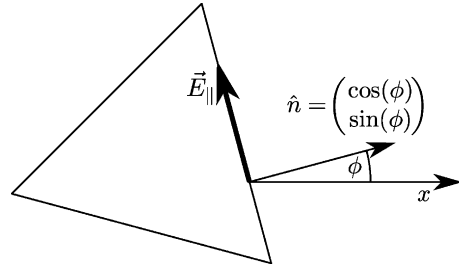


Fig. 1. Physical interpretation of the effective permittivity. We consider the electric field component parallel to an edge of a triangle. Rotating the system in a way that the normal vector coincides with the x -axis allows us to connect the projection of $\underline{\epsilon}^{-1}$ on \vec{E}_\parallel with the effective permittivity we need for the numerical flux.

tive permittivity

$$\epsilon_{\text{eff}} = \frac{\det \underline{\epsilon}}{\hat{n}^T \underline{\epsilon} \hat{n}}$$

which accounts for all necessary modifications.

Besides this rigorous derivation, an easy physical interpretation is readily available. Consider the numerical flux through an edge of a triangle as shown in Fig. 1. The vector normal to this edge is given by

$$\hat{n} = \begin{pmatrix} \cos(\phi) \\ \sin(\phi) \end{pmatrix}$$

We are interested in the propagation of fields along the normal. Hence, we identify the electric field component E_\parallel parallel to the edge as the relevant component for the propagation. After a rotation of the system around the z -axis by $-\phi$, the normal vector is parallel to the x -axis. For the inverse permittivity in the new system we obtain:

$$\begin{aligned} \tilde{\epsilon}^{-1} &= \mathcal{R}(-\phi) \underline{\epsilon}^{-1} \mathcal{R}^T(-\phi) \\ &= \frac{1}{\det(\underline{\epsilon})} \cdot \mathcal{R}(-\phi) \begin{pmatrix} \epsilon_{yy} & -\epsilon_{xy} \\ -\epsilon_{yx} & \epsilon_{xx} \end{pmatrix} \mathcal{R}^T(-\phi). \end{aligned}$$

Here $\mathcal{R}(-\phi)$ denotes the two-dimensional rotation matrix for the angle $-\phi$. After evaluating the matrix products, we find the identity

$$\epsilon_{\text{eff}} \equiv \frac{1}{(\tilde{\epsilon}^{-1})_{22}}.$$

Thus, the inverse effective permittivity is essentially the projection of the inverse epsilon tensor on the direction of the electric field component parallel to the edge of an element.

Please note that the rigorous derivation can be applied to three-dimensional systems as well. However,

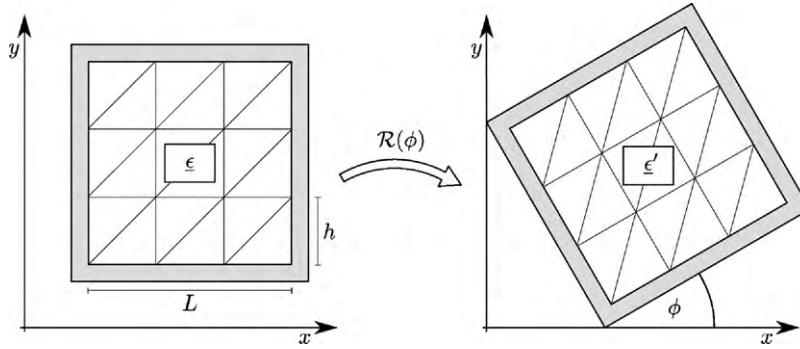


Fig. 2. The setup used for the validation of our implementation of anisotropic materials. The left-hand side shows a square cavity of side length L filled with a material with permittivity ϵ which is bounded by a perfect electric conductor. The cavity is tessellated into a number of congruent triangles characterized by a side length h . This system translates into the own shown at the right-hand side by rotating it through an angle ϕ . Thereby, the permittivity tensor changes and acquires off-diagonal components. In turn, this provides us with a robust test case for a general anisotropy.

one has to account for two distinct polarisations normal to a propagation direction \hat{n} , which significantly complicates matters. In particular, the physical interpretation cannot hold in its current form as polarisation effects are not considered so far. Nevertheless, ongoing investigations hint that these can be accounted for by minor modifications.

4. Validation

To verify our method for anisotropic materials, we investigate the square cavity $(x, y) \in [0, L]^2$ as shown in Fig. 2. The cavity is filled with an anisotropic material characterized by

$$\underline{\epsilon} = \begin{pmatrix} \epsilon_{xx} & 0 \\ 0 & \epsilon_{yy} \end{pmatrix}.$$

The boundary of the cavity is a perfect electric conductor, i.e., the electrical field component tangential to the boundary vanishes. For any given time t , the field distribution within the cavity for the (1, 1)-mode is given by

$$\begin{aligned} E_x(\vec{x}, t) &= \frac{-\pi}{\omega L \epsilon_{xx}} \cdot \cos\left(\frac{\pi}{L}x\right) \cdot \sin\left(\frac{\pi}{L}y\right) \cdot \sin(\omega t) \\ E_y(\vec{x}, t) &= \frac{\pi}{\omega L \epsilon_{yy}} \cdot \sin\left(\frac{\pi}{L}x\right) \cdot \cos\left(\frac{\pi}{L}y\right) \cdot \sin(\omega t) \\ H_z(\vec{x}, t) &= \cos\left(\frac{\pi}{L}x\right) \cdot \cos\left(\frac{\pi}{L}y\right) \cdot \cos(\omega t), \end{aligned} \quad (3)$$

where

$$\omega = \frac{\pi}{L} \cdot \sqrt{\frac{1}{\epsilon_{xx}} + \frac{1}{\epsilon_{yy}}}.$$

However, with this simple test we can only validate our method for diagonal permittivity tensors. For a full

validation, we rotate the entire system by an angle ϕ . In the rotated system, the cavity is filled with a material

$$\epsilon' = \mathcal{R}(\phi) \epsilon \mathcal{R}(\phi)^T.$$

Again, $\mathcal{R}(\phi)$ denotes the rotation matrix. Thus, in the x - y coordinate system the rotated cavity is filled with an anisotropic material with (in general) non-vanishing, identical off-diagonal elements. The analytical solution of this system is given by a mere rotation of (3).

We initialize the fields in our numerical simulation with the respective analytical values for the (1, 1)-mode at $t = 0$. Using the DGTD method, we evolve the fields in time for various orders p of the Lagrange polynomials and different element sizes h . For the time stepping, we

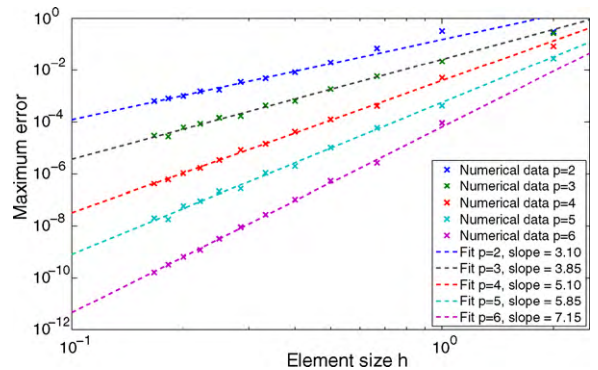


Fig. 3. Numerical errors for the H_z component of the (1, 1)-mode in a cavity rotated by 30° . For the material we used $\epsilon_{xx} = 4$ and $\epsilon_{yy} = 2.0$ and transferred the permittivity tensor into the rotated system. The crosses indicate the deviations from the numerical solution to the analytical one for different element sizes h (as defined in Fig. 2). The colours represent different orders p of Lagrange polynomials. The dashed lines are the results of linear fitting procedures which favour smaller values of h . (For interpretation of the references to colour in this figure legend, the reader is referred to the web version of the article.)

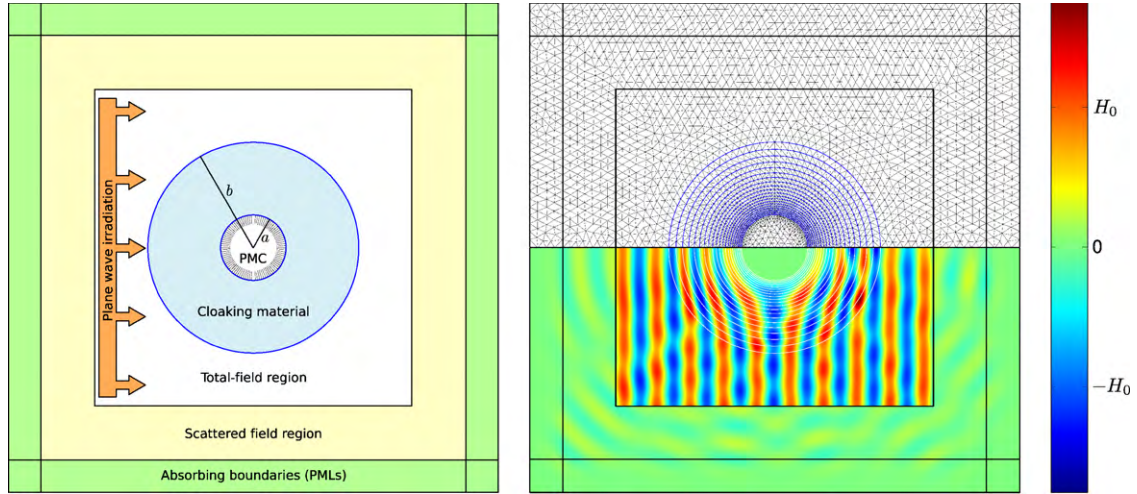


Fig. 4. Left panel: Sketch of the simulation setup. Using the total-field/scattered-field technique, a plane wave is launched onto a cylindrical cloak which surrounds a perfect magnetic conductor. Right panel: The upper part shows the triangular mesh used for the simulation. The cloak is composed by 20 rings of decreasing width. The lower part shows the magnetic field for a plane wave with $\lambda = a = 632.8$ nm. The colours indicate the strength of the magnetic field, where H_0 is the amplitude of the incident plane wave. A good fraction of the wave is reflected into the scattered-field region.

use a fourth-order Runge–Kutta solver. Due to the explicit nature of this solver, the time step is bounded by Δt_{\max} to maintain numerical stability. To minimise the error of the time integration, we choose a small time step $\Delta t = 0.05 \cdot \Delta t_{\max}$ and simulate about 14 optical cycles. At each time step, we calculate the error as the maximum deviation of the numerically obtained magnetic field and the analytical reference within the cavity. The total error of the simulation is then defined by

$$\text{Error} = \max_i \left(\max_{\vec{x} \in [0, L]^2} |H_z^{\text{num}}(\vec{x}, i\Delta t) - H_z^{\text{ana}}(\vec{x}, i\Delta t)| \right).$$

Fig. 3 shows the error in dependence of h and p . We observe that the exponential convergence of the isotropic case [3],

$$\text{Error} \propto h^{p+1},$$

is nicely reproduced even for anisotropic materials. Thus, we conclude that our algorithm is at least working for experimentally relevant symmetric permittivity tensors. Nevertheless, as in the course of the derivation we only assume that $\underline{\epsilon}$ is invertible, the extension should hold for even more general permittivities.

5. Optical cloaking

As a stress test for our method we want to apply it to optical cloaking [9,10]. The idea is to coat an obstacle with a specially tailored material layer which guides

light around it. Ideally, the shape of the incident light wave is recovered behind the scatterer. As an observer cannot distinguish between the recovered wave and the original one, the object is invisible.

In order to achieve optical cloaking, the material layer usually has uncommon properties. In particular, the permittivity of the material continually changes with position. Furthermore, the materials generally show anisotropic behaviour. However, such materials do not exist in nature. Therefore, one relies on artificially created metamaterials, whose substructures cannot be resolved by incident radiation and, hence, act as effective media. A variation of the substructure allows for a change in the material parameters, rendering intriguing properties possible. While this problem is experimentally very challenging, it also imposes great problems on numerical simulations.

Let us consider a cylindrical shell of inner radius a and outer radius b as shown in Fig. 4. The shell consists of a material with [10]:

$$\begin{aligned} \mu_z = 1, \epsilon_\phi &= \left(\frac{b}{b-a} \right)^2, \quad \text{and} \\ \epsilon_r &= \left(\frac{b}{b-a} \right)^2 \left(\frac{r-a}{r} \right)^2 \end{aligned} \tag{4}$$

and is illuminated by TE-polarised light. We note that the permittivity is given in a cylindrical coordinate system whose origin coincides with the shell’s centre with azimuthal and radial components ϵ_ϕ and ϵ_r , respectively. Most strikingly, ϵ_r vanishes as the distance r

to the center of the shell approaches a . As a consequence, the phase speed diverges to infinity. Furthermore, Eq. (4) describes a non-dispersive material. In principle, the inclusion of dispersive materials in the DGTD framework is straightforward via auxiliary differential equations [1]. However, such an extension is beyond the scope of this paper, which focusses on the technical challenges of the dielectric, numerical flux-modifying contributions of anisotropic materials.

In our simulations, we model the cylindrical cloak by a series of 20 rings. Each ring is approximated by homogeneously filled triangles, i.e., the anisotropic material properties are constant within a triangle and are determined by the position of its centre according to (4). Though this does not represent ideal, continuously varying parameters, we argue that this is a good approximation to the experimental situation, where one would change the material by varying the material composition of finite-sized unit cells. The outermost ring is five times as thick as the innermost ring to account for the drastic changes near the inner boundary. As an obstacle, we fill the inside of the shell with a perfect magnetic conductor (PMC). We illuminate our system by a plane wave of wavelength λ via the established total-field/scattered-field technique [1]. Perfectly matched layers [5] absorb light which is scattered by the cloak/PMC system. For the geometrical parameters we choose $\lambda = a = 632.8$ nm and $b = a/0.314$.

To speed up the simulations, we exploit the mirror symmetry of the system. Our mesh is depicted in Fig. 4. Third-order Lagrange polynomials are used as local basis functions. To maintain numerical stability, the time step is reduced by the maximum phase speed in the system according to the CFL criterion [1]. For our discretisation, this is a factor of about 50.

Fig. 4 also features a colour plot of the magnetic field. The total-field region shows what an observer would see. The scattered-field region reveals all deviations of the resulting field to an ideal plane wave due to scattering off the optical cloak and the enclosed PMC. In the case of perfect cloaking, an undisturbed plane wave would be expected in the total-field region, while no field should be present in the scattered-field region. Though deviations are obvious, the overall performance of the cloak seems acceptable as the plane wave shape is approximately recovered once the wave has passed the scatterer. To further quantify the quality of the cloak, we calculate its scattering cross-section per unit length by integrating the energy flux on a closed contour in the scattered-field region and compare it to that of the PMC alone, i.e., without the

cloak. We obtain

$$C_{\text{scat}}^{\text{PMC}} \approx 2890 \text{ nm}, \quad \text{and} \quad C_{\text{scat}}^{\text{cloak}} \approx 464 \text{ nm}.$$

Thus, the cloak reduces the amount of scattered light by a factor of approximately 6.2. The performance of the cloak is fundamentally limited by the chosen material parameters (4), which are impedance mismatched at the outer cloak boundary [10]. Hence, some light is scattered away before the cloak can actually start to guide the light around the obstacle. Secondly, the performance of the cloak is further limited by the size of the unit cells used to generate the desired material parameters. As the permittivity abruptly changes from unit cell to unit cell, inter-cell scattering inevitably occurs and impedes the cloaking effect. Finally, the diverging material parameters at the inner boundary cannot be achieved in practice. To assess the dominant contribution to the scattering cross-section, we repeat our simulations for 10, 15, and 25 rings. We find that the scattering cross-section is nearly independent of the number of rings with the relative difference between the maximum and the minimum cross-section being below 0.3%. We conclude that the impedance mismatch at the outer boundary is the main factor which impairs the performance of the cylindrical cloak. The overall cloaking effect is still visible for surprisingly few rings.

As a last note, we want to mention that time-domain simulations might not be ideal for such kinds of simulations. Tests with radially independent material parameters indicate that it is crucial to properly resolve the material parameters at the inner boundary. The critical time step Δt is limited by the smallest triangle size h and the (inverse) maximum speed of light c . As we increase the resolution near the inner cylinder, the triangle centres approach the boundary as well. Thus, h decreases at the same time as c increases. Both effects decrease the time step and drastically increase the computational overhead. For such situations, frequency-domain calculations are more appropriate. To this end, we have developed a frequency-domain version of our Discontinuous Galerkin method, details of which will be published elsewhere.

6. Conclusion and outlook

We have presented an extension to the DGTD method for Maxwell's equations to include anisotropic materials in two-dimensional transverse-electric polarisation. We have shown that the update equations undergo simple modifications. Changes to the numerical flux are accounted for by an effective permittivity

for the electric field component tangential to the edge of an element. Our extension conserves the superior convergence properties of the original method. We have applied our method to an optical cloaking device and have observed pronounced scattering for realistic setups. For the future, a three-dimensional formulation and the application to other physical problems will be interesting.

Acknowledgements

We acknowledge financial support by the Center for Functional Nanostructures (CFN) of the Deutsche Forschungsgemeinschaft (DFG) within subproject A1.2. The research of MK is further supported through the Karlsruhe School of Optics & Photonics (KSOP) at the Karlsruhe Institute of Technology (KIT) and the Studienstiftung des Deutschen Volkes. The Young Investigator Group of JN received financial support by the “Concept for the Future” of the KIT within the framework of the German Excellence Initiative.

References

- [1] A. Taflov, S.C. Hagness, *Computational Electrodynamics: The Finite-Difference Time-Domain Method*, 3rd ed., Artech House Publishers, 2005.
- [2] J. Jin, *Computational Electrodynamics: The Finite Element Method in Electromagnetics*, 2nd ed., John Wiley & Sons, 2002.
- [3] J. Hesthaven, T. Warburton, Nodal high-order methods on unstructured grids. I. Time-domain solution of Maxwell’s equations, *J. Comput. Phys.* 181 (1) (2002) 186–221.
- [4] J.S. Hesthaven, T. Warburton, *Nodal Discontinuous Galerkin Methods: Algorithms, Analysis, and Applications*, Springer, 2008.
- [5] T. Lu, P. Zhang, W. Cai, Discontinuous Galerkin methods for dispersive and lossy Maxwell’s equations and PML boundary conditions, *J. Comput. Phys.* 200 (2) (2004) 549–580.
- [6] X. Ji, W. Cai, P. Zhang, High-order DGTD methods for dispersive Maxwell’s equations and modelling of silver nanowire coupling, *Int. J. Numer. Meth. Eng.* 69 (2) (2007) 308–325.
- [7] J. Niegemann, M. König, K. Stannigel, K. Busch, Higher-order time-domain methods for the analysis of nano-phonic systems, *Photon. Nanostruct.: Fundam. Appl.* 7 (2009) 2.
- [8] K. Stannigel, M. König, J. Niegemann, K. Busch, Discontinuous Galerkin time-domain computations of metallic nanostructures, *Opt. Exp.* 17 (17) (2009) 14934–14947.
- [9] J. Li, J.B. Pendry, Hiding under the carpet: a new strategy for cloaking, *Phys. Rev. Lett.* 101 (20) (2008) 203901.
- [10] W. Cai, U.K. Chettiar, A.V. Kildishev, V.M. Shalaev, Optical cloaking with metamaterials, *Nat. Photon.* 1 (2007) 224–227.
- [11] U. Leonhardt, T. Tyc, Broadband invisibility by non-euclidean cloaking, *Science* 323 (5910) (2009) 110–112.
- [12] S. Chun, J. Hesthaven, High-order accurate thin layer approximations for time-domain electromagnetics. Part I. General metal backed coatings, *J. Comput. Appl. Math.* 231 (2) (2009) 598–611.
- [13] R. Diehl, K. Busch, J. Niegemann, Comparison of low-storage Runge–Kutta schemes for discontinuous Galerkin time-domain simulations of Maxwell’s equations, *J. Comput. Theor. Nanosci.*, in press.
- [14] R.J. LeVeque, *Finite Volume Methods for Hyperbolic Problems*, Cambridge University Press, 2002.